Fast-wave power flow along SOL field lines in NSTX and the associated power deposition profile across the SOL in front of the antenna

IOP PUBLISHING and INTERNATIONAL ATOMIC ENERGY AGENCY

NUCLEAR FUSION

Fast-wave power flow along SOL field lines in NSTX and the associated power deposition profile across the SOL in front of the antenna

R.J. Perkins[1], **J.-W. Ahn**[2], **R.E. Bell**[1], **A. Diallo**[1], **S. Gerhardt**[1],
T.K. Gray[2], **D.L. Green**[2], **E.F. Jaeger**[3], **J.C. Hosea**[1],
M.A. Jaworski[1], **B.P. LeBlanc**[1], **G.J. Kramer**[1], **A. McLean**[2],
R. Maingi[1], **C.K. Phillips**[1], **M. Podestà**[1], **L. Roquemore**[1],
P.M. Ryan[2], **S. Sabbagh**[4], **F. Scotti**[1], **G. Taylor**[1] and **J.R. Wilson**[1]

[1] Princeton Plasma Physics Laboratory, Princeton, NJ, USA
[2] Oak Ridge National Laboratory, Oak Ridge, TN, USA
[3] XCEL Engineering Inc., Oak Ridge, TN, USA
[4] Department of Applied Physics and Applied Mathematics, Columbia University, New York, NY, USA

E-mail: rperkins@pppl.gov

Abstract

Fast-wave heating and current drive efficiencies can be reduced by a number of processes in the vicinity of the antenna and in the scrape-off layer (SOL). On NSTX from around 25% to more than 60% of the high-harmonic fast-wave power can be lost to the SOL regions, and a large part of this lost power flows along SOL magnetic field lines and is deposited in bright spirals on the divertor floor and ceiling. We show that field-line mapping matches the location of heat deposition on the lower divertor, albeit with a portion of the heat outside of the predictions. The field-line mapping can then be used to partially reconstruct the profile of lost fast-wave power at the midplane in front of the antenna, and the losses peak close to the last closed flux surface as well as the antenna. This profile suggests a radial standing-wave pattern formed by fast-wave propagation in the SOL, and this hypothesis will be tested on NSTX-U. RF codes must reproduce these results so that such codes can be used to understand this edge loss and to minimize RF heat deposition and erosion in the divertor region on ITER.

(Some figures may appear in colour only in the online journal)

1. Introduction

Plasma heating using waves in the ion-cyclotron range of frequencies (ICRFs) is a primary heating scheme on ITER, where up to 20 MW of ICRF power is planned [1]. Effectively coupling the ICRF power from the sources to the core plasma is a major goal, and traditional issues include: (1) maintaining high antenna loading by keeping the gap between the plasma separatrix to the antenna as small as possible and/or the edge density as large as permitted; (2) losses near the antenna structures such as RF-sheath enhanced bombardment [2, 3]; (3) parametric decay instability (PDI) [4, 5]; (4) and multi-pass damping where waves that penetrate the core damp out at the plasma edge [6]. However, high-harmonic fast-wave (HHFW) heating experiments on the National Spherical Torus eXperiment (NSTX) show that significant losses can also occur

directly in the scrape-off layer (SOL) as the waves propagate away from the antenna [7–11]. These SOL losses occur prior to the RF power reaching the core plasma because multi-pass damping is likely negligible on NSTX due to its high beta and subsequent high single-pass absorption [7, 8, 12]. Such losses can create situations of poor core heating even with relatively high antenna loading, and such effects must be taken into account in conjunction with any subsequent multi-pass damping that may occur in cases of lower single-pass absorption. For reference, the NSTX HHFW system operates at 30 MHz, contains twelve straps for variable phasing, and possesses a boron-nitride Faraday shield (see [13, 14] for details).

Previous work relates HHFW interaction with the SOL to reduced heating and current-drive efficiencies [7, 8]. The SOL interactions are evident in camera images such as in figure 1
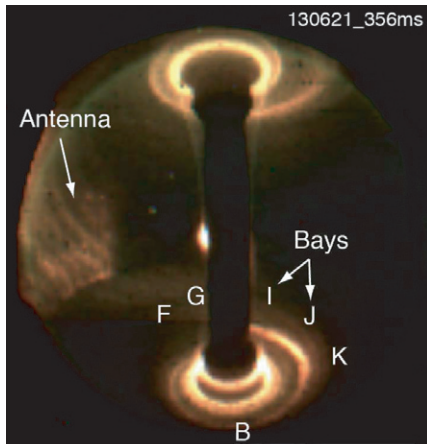
Figure 1. Strong interactions of the HHFW power and the edge plasma are clearly seen in this midplane visible-light image of the spirals on the upper and lower divertor for an ELM-free H-mode plasma with $P_{RF} = 1.8$ MW. The conditions for shot 130621 are: $\phi_{ANT} = -90°$, $P_{NB} = 2$ MW, $I_P = 1$ MA, $B_\phi = 0.55$ T.
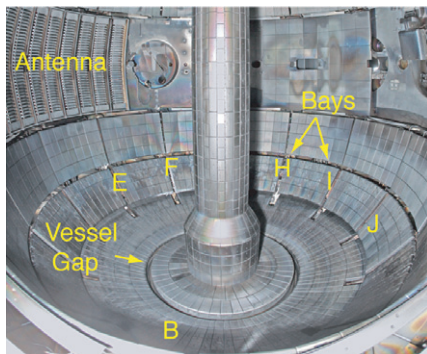
Figure 2. Vessel image showing position of the antenna, tiles, vessel gap [15] and toroidal bay locations. View rotated 30° toroidally relative to that of figure 1.

(comparable in-vessel view in figure 2), where bright streaks emanate from the antenna region and terminate on the upper and lower divertor in bright and hot spirals [9, 10]. Figure 1 shows the spirals for the $k_\phi = -8$ m^{-1} ($-90°$ phasing between antenna straps) case of shot 130621 for which approximately 40% of the RF power coupled from the antenna reached the core plasma, meaning that approximately 60% was lost to the SOL (see figure 4 in [9]). Infrared (IR) camera measurements of these spirals show a significant RF-produced heat flux to the divertor region, up to ~ 2 MW m^{-2} for an RF coupled power of 1.8 MW [10]. This indicates that a significant part of the HHFW power missing from the core is coupling directly to the SOL and is being deposited on the divertor floor and ceiling. The heating efficiency is a strong function of the toroidal wavenumber, k_ϕ, selectively launched at the antenna, and edge density [7–10]. Importantly, the flow of the HHFW power from the midplane to the divertor regions in the SOL is largely along field lines [11], as has been determined by field-line mapping using the SPIRAL code [16], and occurs along all SOL field lines passing in front of the antenna between the antenna and the last closed flux surface (LCFS) and not just those connected to antenna components.

In this paper, we estimate the radial profile of lost HHFW power across the SOL midplane in front of the antenna by using the field-line mapping to map the IR divertor measurements of RF-produced heat flux back to the midplane. For the case of figure 1, this procedure yields a power profile with relatively strong coupling approximately 1 cm inboard of the antenna and again a few millimetres outboard of the LCFS and relatively weak coupling in between. This shows that the underlying mechanism behind this power loss to the divertor regions is not localized to the antenna components and is distinct from and in addition to the RF-sheath losses at the components as described in [2, 3]. We hypothesize that the underlying mechanism is fast-wave propagation in the SOL, with the low-density plasma between the antenna and LCFS acting in effect as a waveguide. Evidence for this behaviour is found in the relationship between heating efficiency, edge density, and the location of the onset density for perpendicular fast-wave propagation (i.e. the right-hand cutoff) [7, 8], and the loss profiles obtained here suggest a radial standing-wave pattern in the SOL channel between the very steep density gradient at the LCFS and the perpendicular fast-wave cutoff/vessel wall. Future modelling and experiments on NSTX-U will be required to determine definitively the contribution of fast-wave propagation in the SOL to the RF-power loss against the possible contributions from reactive fields/currents excited in front of the antenna and from energetic ions produced by PDI. The results presented here are important for verifying RF codes that include the SOL region [17], as these codes must be able to reproduce these edge losses under NSTX conditions. Once such codes can predict the amount of fast-wave power coupled to the SOL, they can be used for determining the underlying cause(s) and for understanding how to minimize this direct SOL power loss for fast-wave heating, generally.

2. Field-line mapping and HHFW power flow in the SOL

HHFW power lost in the SOL flows mainly along the magnetic field, as is evidenced by comparing SOL field-line mapping to various measurements of RF-produced effects in the divertor regions [11]. The following sections describe the field-line mapping procedure and its uncertainties.

Field-line mapping is done using the SPIRAL code, a full-orbit particle code [16]. The particle orbits produced with SPIRAL can be taken as proxies for the field lines because the particles are launched here with velocities parallel to the magnetic field, which minimizes grad-B drifts, and with low speeds (1 eV deuterons), which minimizes curvature drifts. In this paper, field lines are tracked from the midplane in front of the antenna (which has a 90° toroidal span) to the point at which they strike the divertor region. Let R_{SOL} denote the major radius of a field line at the midplane. Figure 3 then provides a top-down view of three sets of field lines with selected R_{SOL} of 1.57, 1.55 and 1.51 m that lie between the antenna radius of 1.575 m and the LCFS radius of 1.477 m. Each set contains twenty field lines that cover the 90° toroidal span of the antenna. The points at which the field lines strike the lower divertor are denoted by squares. Although the antenna spans 90°, the lines converge radially as they wind around the centre column, and lines starting closer to the LCFS strike the divertor farther in radially and wrap around the centre column more
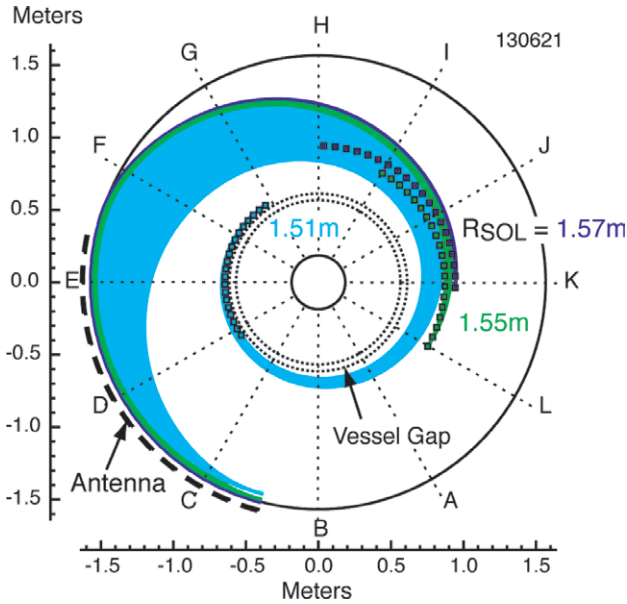
Figure 3. Field lines mapped between the midplane in front of the antenna and the lower divertor. The squares denote the points at which each field line strikes the divertor, and letters denote bays. The different colours denote lines that start at different radii at the midplane. Field lines starting more inboard of the antenna spiral around more and reach in further radially.
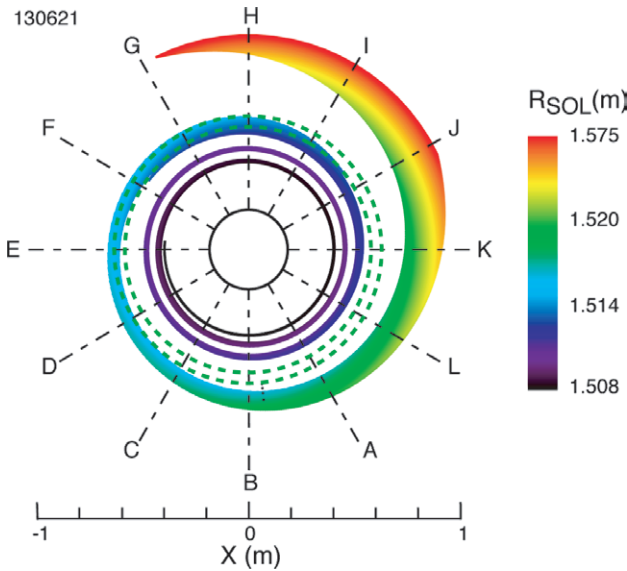
Figure 4. A large set of strike points defines a large spiral on the divertor floor. Field lines are tracked from the midplane in front of the antenna; the colour-coding denotes the midplane radii of each line. The resulting spiral matches those seen in camera images (figure 1). The vessel gap is denoted by the dashed green circles.

toroidally, generating a spiral pattern similar to the visible-camera image in figure 1.

It is often sufficient to know only the strike points of the field lines rather than the entire trajectories. Figure 4 plots these strike points on the lower divertor floor for a much-denser set of field lines that includes many different R_{SOL}; the colour-coding denotes the midplane radius of the field line from which each strike point originated. The set of strike points forms a spiral as is observed experimentally (figure 1). It is

important to not confuse this spiral, formed by a collection of field-line strike points, with the spiralling SOL field-line trajectories shown in figure 3. The strike-point positions allow quantitative comparisons of RF-induced effects with the field-line mapping.

Previous comparisons of the field-line mapping to diagnostic measurements showed that the HHFW power flow through the SOL is largely field-aligned. The RF-spiral moves across the divertor radially at a given toroidal location when the magnetic pitch of NSTX is changed as is observed in visible-camera images and in signals from Langmuir probes and current-sensing tiles [11]. The computed strike points reproduce this motion and reveal that the spiral movement is actually a rotation of the spiral due to the altered magnetic pitch. Moreover, the calculated strike points for the first pass of the spiral lie over Langmuir probes or current-sensing tiles on those shots for which the diagnostics show a strong response to the RF pulse, further demonstrating that the HHFW power flows through the SOL to the divertor region essentially along the magnetic field.

Uncertainties in the field-line mappings arise from the equilibrium fits. Two reconstructions, both of which utilize external magnetic measurements, are typically available: NSTX EFIT (EFIT02) [18], a partial kinetic analysis that is additionally constrained by electron pressure and diamagnetic loop measurements, and LRDFIT [19] constrained by the electron temperature (LRDFIT04). The fits also differ in how they treat currents in the vessel structure, which are known to impact the location of the outer vessel strike radius [20]. Also, the list of magnetic measurements used in each fit can differ for the same shot, leading to different results. In general, the two fits can produce strike points that differ by up to a few centimetres at a given toroidal location at inner radii approaching the outer vessel strike radius. For instance, figure 5 compares the field-line mapping produced by both fits against lower divertor optical (Li i) emission for shot 141899 [21]. The image has been inverted and plotted as major radius versus toroidal angle [22]. The EFIT02 strike points fit the emission better at outer radii and just inside the vessel gap but eventually deviate at inner radii. LRDFIT04 does not fit as well at outer radii but fits better as the outer vessel strike radius is approached. These differences are relatively small as observed and do not alter the conclusion that the computed strike points generally coincide with the emission measurements. Note that there is greater uncertainty for strike points at inner radii because such points come from field lines close to the LCFS that make many loops around the X-point where the poloidal magnetic field becomes small. The relative error in the poloidal field is thus large and also sampled repeatedly for such field lines. In conclusion, the field-line mapping is sensitive to uncertainties in the equilibrium reconstructions, and, while the mappings still generally agree with the data, such uncertainties could be important, for example, in specifying exactly the location of the outer vessel strike radius.

3. Comparing magnetic field-line mapping to IR camera measurements in the lower divertor
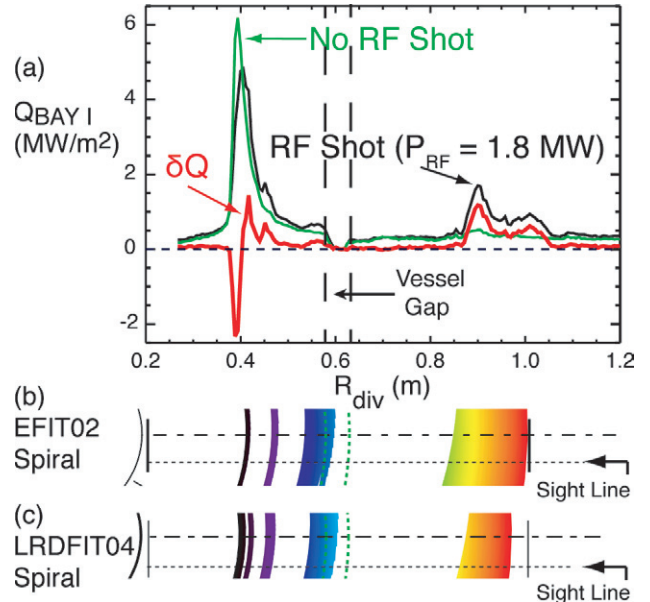
IR cameras aimed at the divertor regions provide valuable information concerning the nature of the RF losses in the
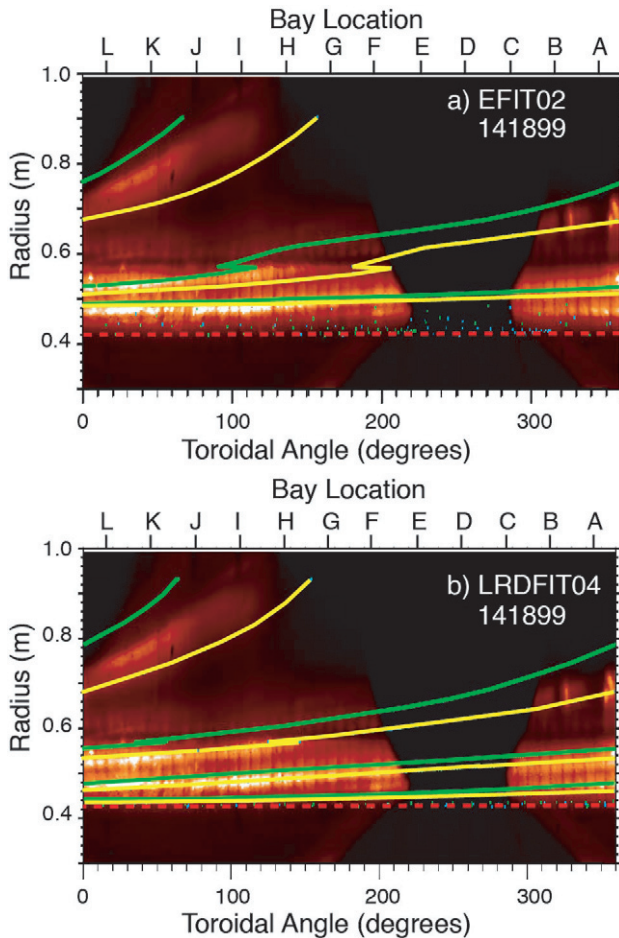
Figure 5. A divertor camera image of Li i emission is overlayed with field-line strike points from (*a*) EFIT02 and (*b*) LRDFIT04. Green points denote field lines from the right side of the antenna, and yellow points from the left hand side, so the RF-power deposition occurs between the yellow and green points.

Figure 6. The field-line strike points agree well with the radii of peak RF-power deposition measured with IR cameras. (*a*) Radial heat-flux profile at bay I both with RF (shot 130621, black) and without RF (shot 130617, green) plotted against divertor radius (R_{div}). Subtraction of the two gives δQ, the RF-power deposition (red). Computed strike points at bay I with (*b*) EFIT02 and (*c*) LRDFIT04. $\phi_{ANT} = -90°$, $P_{NB} = 2\,MW$, $I_P = 1.0\,MA$, $B_{tor} = 0.55\,T$.

SOL. The camera data show the multiple passes of the spiral across a given toroidal location, show that the radial position of these passes is in good agreement with the field-line mapping, and show the spiral motion as the magnetic pitch is changed. Additionally, the camera data provide important insight into the variation of the magnitude of the RF losses along the spiral, which will be exploited in the following section.

The IR camera used in this paper is located at bay I and is aimed at the lower divertor region. An IR camera is positioned to view the upper divertor region at bay G, but at this position the measurements are relatively low for the cases considered, and this paper thus focuses on the lower divertor data. The camera has been calibrated to convert the measured IR emission from a graphite surface into a surface temperature; technical details and calibration procedures can be found in [23]. Using the THEODORE code [24, 25], the time history of the surface temperature is converted into a heat flux normal to the surface. The THEODORE code includes a small layer of poorly conducting material to model the surface layers deposited on the graphite tiles. The heat conduction factor used for the surface layer is typically the smallest value that does not give spurious negative heat-flux values. Lithium wall conditioning was used for the shots analysed

here; lithium effectively reduces the emissivity of the graphite tiles and also forms various compounds that are continuously re-deposited during a discharge. The heat conduction factor used by THEODORE is constant over an IR camera image, but the actual surface-layer conduction may vary spatially. These issues introduce an uncertainty of approximately 10–20% into the absolute calibration of the heat-flux data reported here.

The heat flux measured with IR cameras contains both the RF-produced heat flux and the heat flux ordinarily expelled from the plasma core. However, if a reference shot with identical plasma parameters but no applied RF power is available, then the RF-produced heat flux can be isolated by subtraction. Figure 6 shows heat-deposition profiles along an approximately radial sight line at bay I for two shots under identical ELM-free H-mode conditions: shot 130621 with 1.8 MW of HHFW power and $-90°$ phasing between antenna current elements ($k_\phi = -8\,m^{-1}$), and reference shot 130617 with no HHFW power [9]. Subtracting the two heat profiles gives the RF-induced component of the heat-deposition profile, δQ. The relatively large negative dip in δQ near $R_{div} \sim 0.4\,m$ in figure 6(*a*) is most likely due to a shift in plasma exhaust in the vicinity of the outer vessel strike radius due to RF core heating; this shift makes the subtraction inaccurate for obtaining the peaks of the spiral deposition in the vicinity of the vessel outer strike radius. The subtraction is valid elsewhere and three RF-induced heat peaks are clearly resolved. There is significant heat deposition at large radii, 0.85–1.1 m, well outboard of the outer vessel strike radius. This location is in good agreement with location of the outer band of the strike points shown in figures 6(*b*) and (*c*) for the equilibrium fits EFIT02 and LRDFIT04, respectively. The second pass of the spiral is just inboard of the vessel gap at 0.53–0.6 m, and the

4
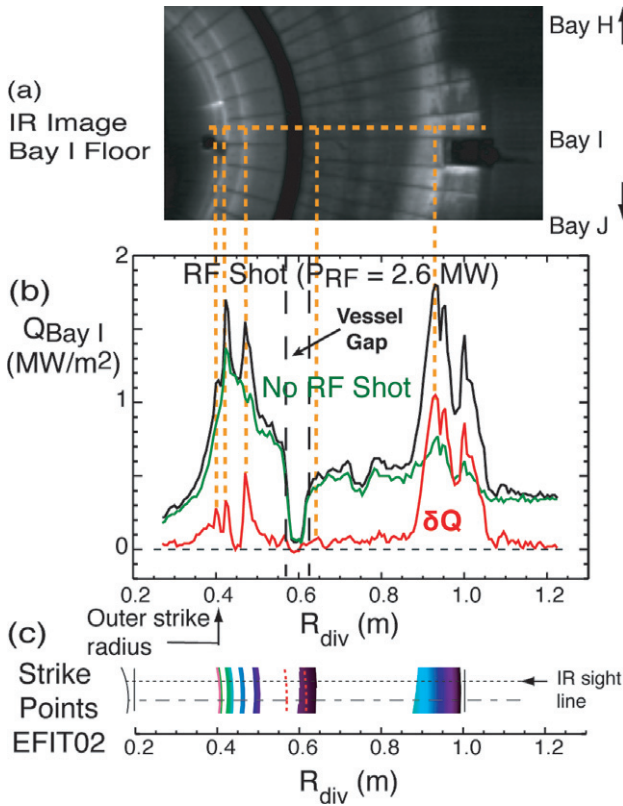
Figure 7. RF heat peaks agree with field-line strike points for an ELMy H-mode plasma (shot 135333, no RF shot 135334). (*a*) Heat-flux image in which multiple passes of the spiral are identifiable. (*b*) A radial profile of heat flux plotted against divertor radius ($R_{\rm div}$). (*c*) Computed strike points at bay I. $\phi_{\rm ANT} = -90°$, $P_{\rm NB} = 2$ MW, $I_{\rm P} = 0.8$ MA, $B_{\rm tor} = 0.45$ T.

corresponding heat deposition is much weaker. An additional heat peak with larger amplitude is clearly resolved at an inner radius of 0.45 m, corresponding to a third crossing of the spiral at bay I. The SPIRAL results also indicate additional heat peaks close to the outer vessel strike radius that are not resolved in figure 6(*a*).

A clearer view of the spiral heat peaks without a negative dip near the outer vessel strike radius has been obtained for an ELMy plasma in figure 7. The ELMs tend to raise the edge density and thus increase the edge losses [7]. The enhanced edge losses reduce the RF core heating so that the exhaust from the plasma around the outer vessel strike radius is less affected by RF power reaching the core plasma inside the LCFS; however, the direct RF-power deposition in the SOL is enhanced. Also, the toroidal magnetic field is reduced in these shots as compared to the ELM-free case, and the reduced magnetic field is known to decrease HHFW heating efficiency [7]. In this case, the spiral streaks are clearly seen in figure 7(*a*), and the heat-flux peaks in the lower divertor are clearly resolved even near the outer vessel strike radius in figure 7(*b*).

Finally, we compare the field-line mapping to IR camera measurements taken for the magnetic pitch scan analysed in [11]. Figure 8 shows the SPIRAL strike points for two shots of the pitch scan with bay I oriented along the horizontal axis. The sight line along which the IR data are taken is above and parallel to the centreline of bay I as shown. The rotation of
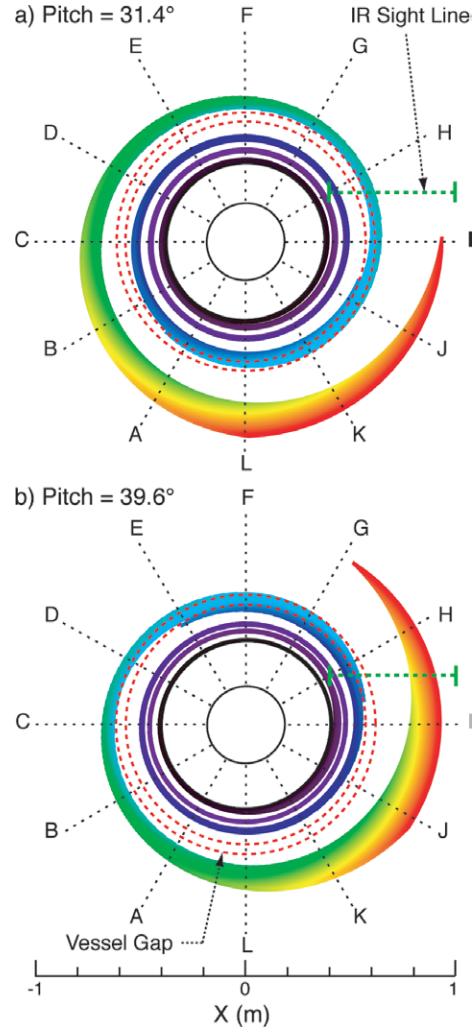
Figure 8. SPIRAL strike points using EFIT02 for the lower divertor floor for different magnetic field pitch (shots 141888 and 141899 at $t = 0.355$ s). As the magnetic pitch increases, the spiral rotates toroidally across the IR sight line ($k_{\rm ANT} = -8$ m^{-1} ($-90°$), D$_2$, $P_{\rm RF} = 1.4$ MW starting at $t = 0.25$ s, $P_{\rm NB} = 2$ MW).

the spiral with pitch is again evident here. Figure 9 compares the IR data to the computed strike points along the sight line near bay I for each shot in the pitch scan; the first and second passes of the spiral are apparent for all shots except 141888, in which only the second pass is visible. IR data were not obtained at smaller radii due to technical difficulties with the camera. Beneath each IR plot are the computed strike points, and the locations of the IR peaks are in good agreement with the field-line mappings. Importantly, the second pass of the spiral moves inward radially with increasing magnetic pitch, as did the first pass in [11], and the strike points track this motion over the gap in the vessel floor. For the low pitch case of shot 141888, the computed strike points do not reach bay I on the first pass as indicated by the absence of strike points at large radii (see figure 8 as well), and there is correspondingly no RF-produced heat flux in the IR data. For shots 141895, 141898 and 141899, there is a substantial additional heat flux outboard of the SPIRAL strike points. The origin of this RF-produced heat flux at such large radii is currently unknown and subject to future investigations, but power flow along field lines
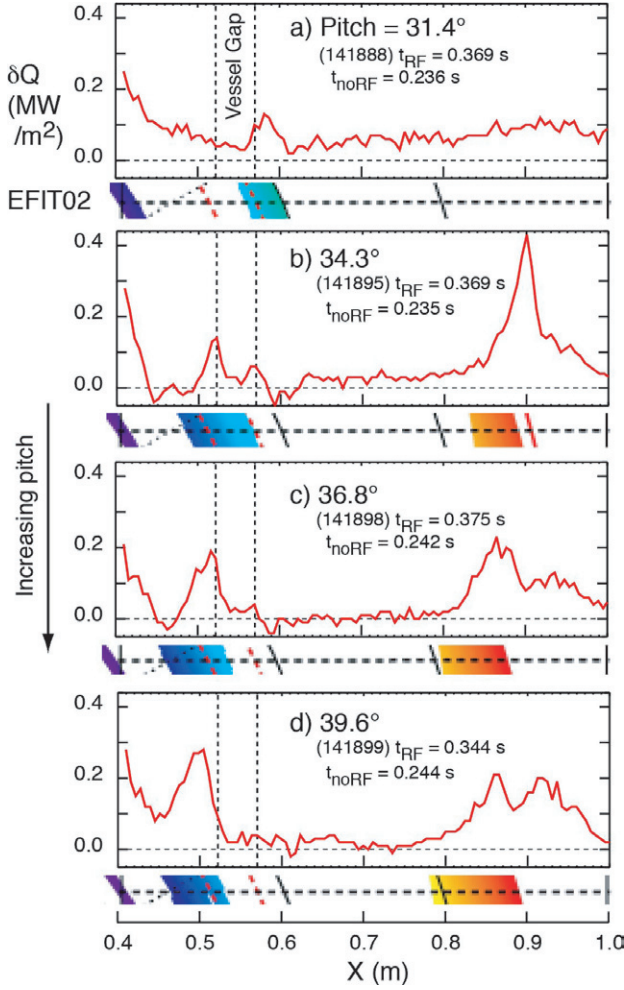
Figure 9. IR data from bay I plotted against X, the distance along the sight line. The positions of the heat peaks generally agree with the field-line mapping. As the magnetic pitch increases, the second spiral pass moves inwards over the vessel gap in both the IR data and the SPIRAL computations. A non-negligible portion of heat lands outside the strike points. The IR data is taken at the times shown and EFIT02 equilibrium fits are taken at 355 ms.

connected to the edge of the antenna bottom plate is suspected. The results presented in figure 9 demonstrate that much of the RF losses to the divertor region follows SOL field lines and that the second heat peak at bay I is generally smaller than the first (outer) heat peak and increases as it moves across the vessel gap towards the LCFS.

4. Calculating the midplane power deposition

Since lost HHFW power flows to the divertor region primarily along field lines, the field-line mapping permits the lower divertor heat flux to be mapped back to the midplane in front of the antenna. This gives a radial profile of the HHFW power lost along different field lines in the SOL and shows that the power lost is relatively high both near the antenna and also the LCFS but drops in between, suggesting a radial standing fast-wave pattern across the SOL. In this analysis, we make the assumption that the RF power lost to the divertor is entirely field-aligned; this is a strong assumption but is supported by the above observations.
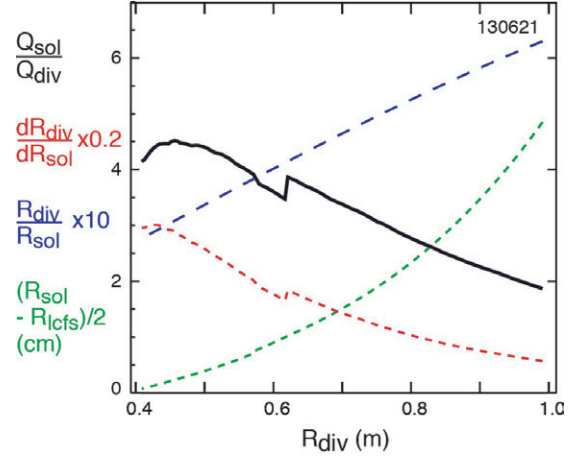
Figure 10. Solid black: the Q_{sol}/Q_{div} factor used to convert power deposited at the divertor region to power coupled along field lines at the midplane. Dotted red: flux expansion. Dashed blue: ratio of radius at divertor to radius at midplane. Dotted green: field-line mapping from divertor to midplane.

We will compute the z-component (vertical component) of the lost RF-power flux at the midplane, Q_{SOL}, from the divertor heat flux using the magnetic field-line mapping. The toroidal component of the lost RF heat flux is unimportant for determining the amount of RF power being deposited in the divertor regions because it is tangential to the divertor surfaces. The THEODORE code returns the component of the heat flux normal to the tile, which can be converted through geometrical factors to the z-component at the lower divertor that we denote simply as Q_{div}. Then, because the lost RF-power flux is assumed divergence-free, there will be a flux expansion factor in going from the divertor to the midplane, as the SOL flux surfaces are more spread out at the divertor than at the midplane due to the weakening of the poloidal field. A horizontal differential surface element on the divertor floor of width dR_{div} at a given divertor radius R_{div} and angular span $d\varphi$ is mapped to another element at the midplane of span $d\varphi$ but at a given SOL radius R_{sol} with width dR_{sol}. Assuming all the RF power flows within the flux tube connecting these two surface elements and that for $dR \ll R$

$$Q_{SOL} R_{SOL} \, d\varphi \, dR_{SOL} = Q_{div} R_{div} \, d\varphi \, dR_{div}. \qquad (1)$$

Thus,

$$Q_{SOL} = Q_{div} \frac{R_{div}}{R_{SOL}} \frac{dR_{div}}{dR_{SOL}}, \qquad (2)$$

where in equation (2) R_{div} is a function of R_{SOL} under the field-line mapping. In figure 10, $R_{sol} - R_{lcfs}$, the radial expansion factor dR_{div}/dR_{sol}, the ratio R_{div}/R_{sol}, and the translation factor Q_{sol}/Q_{div} are plotted as a function of R_{div}. The translation factor Q_{sol}/Q_{div}, calculated using EFIT02, can now be used to calculate Q_{sol} for a given RF-power deposition peak in the divertor region, Q_{div}. Q_{sol}/Q_{div} is relatively large near the outer vessel strike radius (LCFS) and falls off with increasing radius. The jagged portions shown in figure 10 in the vicinity of $R_{div} = 0.6$ m are due to the vessel gap.

Note that only a portion of the lost RF-power profile can be obtained at the midplane because the IR camera used here obtains data from bay I and thus samples only a portion of the
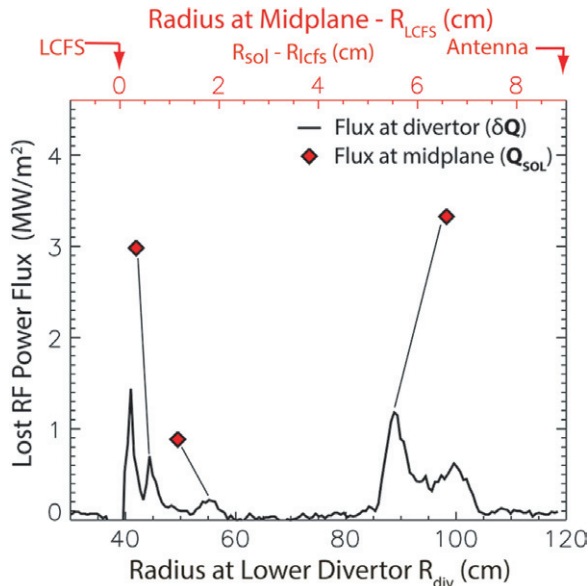
Figure 11. Using the conversion factor shown in figure 10, the IR measurement of RF heat deposition (black curve) can be converted to power lost at the midplane (red points) for the ELM-free case of shot 130621 at $t = 355$ ms. The lost-power profile peaks both close to the antenna and also near the LCFS.
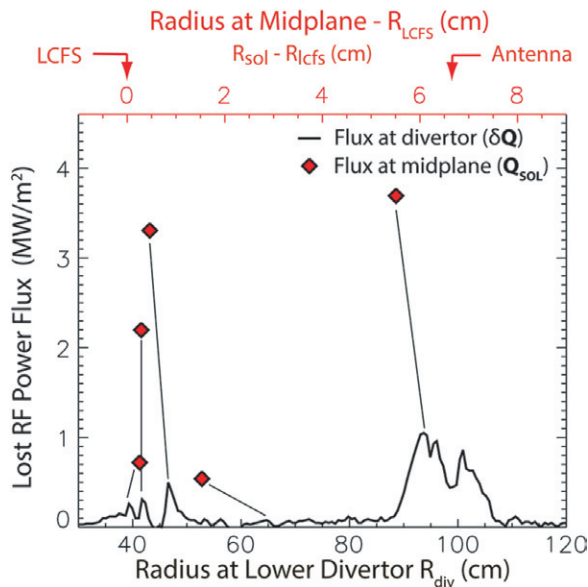
Figure 12. Calculated values of the power lost at the SOL midplane, Q_{sol}, are shown for the peaks of the measured IR profile for the ELMy H-mode plasma (shot 135333). The power lost in the SOL midplane peaks inboard of the antenna and again outboard of the LCFS. ($R_{lcfs} = 1.508$ m).

HHFW power flow, namely that along field lines whose strike points land in the vicinity of bay I. Thus, regions of low heat flux shown in figures 6 and 7 do not necessarily correspond to midplane radii with low lost RF power coupled, as the RF power lost along such field lines lands off of bay I in the lower divertor region. For this reason, only the local maxima of heat flux, where field lines definitely land at bay I, are mapped back to the midplane.

Despite the limitation described above, an indication of the lost-power profile is still obtained, as shown in

figure 11 for the ELM-free case and figure 12 for the ELMy case. In each figure, the lower curve is the δQ obtained above plotted as a function of major radius at the lower divertor. Each peak of these curves is mapped back to the midplane, represented by the upper horizontal axis that is the midplane major radius (R_{SOL}) minus the radius of the LCFS (R_{LCFS}). The interesting conclusion in both cases is that the coupled power is relatively large both close to the antenna and also again near the LCFS. The resolution near the outer vessel strike radius found in the ELMy case shows that the coupled power peaks a few millimetres outboard of the LCFS and a few centimetres inboard of the antenna, which is reminiscent of a standing radial mode. Multiple IR cameras or a single wide-angle lens camera are required to obtain a more complete recovery of the radial loss profile in the SOL.

The observed drop between the antenna and LCFS indicates weak power deposition of the second spiral pass at bay I; the drop is somewhat greater in the ELMy case (figure 12) than in the ELM-free case (figure 11). The IR image of figure 7 faintly shows the second pass just outboard of the vessel gap at the sightline for the IR data, so the weak power deposition is not due to the second pass landing in the vessel gap. Also, this lower value is consistent with the lower spiral intensity indicated in figure 5 just outboard of the vessel gap. Finally, in figure 9 the RF-power deposition for the second pass increases as the pitch is increased, indicating that the deposition increases as this peak is moved closer to the LCFS (shots 141895, 141898 and 141899 have essentially the same plasma density conditions). All of these observations point to a loss profile in the SOL midplane in front of the antenna that peaks near the antenna and near the LCFS and that drops to a relatively low value in between.

5. Conclusions

Given that the HHFW power lost to the SOL flows from the NSTX antenna region to the divertor essentially along field lines, the IR camera data has been mapped back to the midplane to obtain an estimate of the radial profile of lost power across the SOL. In both cases analysed, power is lost strongly to field lines close to the antenna and to the LCFS but not in between. How and where the HHFW power is converted into a heat flux has yet to be determined definitively, but we hypothesize that the underlying mechanism is fast-wave propagation in the SOL [7, 8] and that the bright and hot spirals result from RF-driven sheaths on the divertor plates. The midplane profile of lost HHFW power could then be similar to a radial standing-wave pattern in a cavity due to partial reflections of the waves off the steep pedestal gradient. Direct measurements of RF fields will be needed on NSTX-U to verify fast-wave propagation in the SOL, and modelling of the power coupling to the SOL is required to determine the relative contributions to losses to the divertor from propagating fast waves versus reactively induced fast-wave excitation effects. PDI, another possible mechanism of direct SOL heating in the vicinity of the LCFS [6], also needs to be modelled to determine its contribution to the power deposited in the divertor region. However, initial SPIRAL computations for the energetic ions produced by PDI indicate

that they are mostly mirror trapped away from the divertor regions.

It is not yet possible to calculate the total power lost via the SOL to the divertor region due to the limited toroidal coverage of the IR measurements and the strong toroidal variation in the RF-produced heat flux. However, a very crude estimate of the power deposited can be made using red spectra emission normalized to the maximum Q_{div} amplitude at bay I, as a proxy for the toroidal variation of the Q_{div}. This crude estimate suggests that these field-aligned losses to the divertor regions account for about half of the RF-power loss ($\sim$1.1 MW [9]) in the case of shot 130621, indicating that these field-aligned SOL losses to the divertor are significant but that other losses such as associated with PDI [4, 5] and with sheath losses on antenna components and adjacent structures connected by magnetic field lines [26, 27] undoubtedly make significant contributions as well. Preparations are underway for NSTX-U to greatly increase the toroidal IR coverage in order to quantify the total power lost in the spirals using the measured Q_{div} values.

While the losses to the divertor region along field lines have been studied here on NSTX, a spherical torus with relatively high magnetic pitch, field-aligned ICRF effects in the SOL, such as erosion and impurity production [28–30], have also been observed under conventional-tokamak conditions and indicate these effects are common to fast-wave systems. These losses to the divertor may be more apparent on NSTX because the increased field pitch causes the spiral to be less 'sheared' than in a conventional tokamak, and a low-shear spiral is more readily observed. Importantly, these RF-power losses in the SOL obtained on NSTX provide a clear test for verifying advanced RF codes that treat the SOL region and that in turn can be used to theoretically understand the process(es) underlying the SOL power flow. Such advanced RF codes must include the proper physics to reproduce these losses under NSTX-like conditions before they can be used to predict and possibly minimize SOL power losses to the divertor region on ITER.

Acknowledgment

References

[1]   Swain D.W. and Goulding R.H. 2007 *Fusion Eng. Des.* **82** 603
[2]   Jacquet P. *et al* 2011 *Nucl. Fusion* **51** 103018
[3]   D'Ippolito D.A. *et al* 1988 *Nucl. Fusion* **38** 1543
[4]   Wilson J.R. *et al* 2005 *AIP Conf. Proc.* **787** 66
[5]   Biewer T.M. *et al* 2005 *Phys. Plasmas* **12** 056108
[6]   Petty C.C. *et al* 1999 *Nucl. Fusion* **39** 1421
[7]   Hosea J.C. *et al* 2008 *Phys. Plasmas* **15** 056104
[8]   Phillips C.K. *et al* 2009 *Nucl. Fusion* **49** 075015
[9]   Hosea J.C. *et al* 2009 *AIP Conf. Proc.* **1187** 105
[10] Taylor G. *et al* 2010 *Phys. Plasmas* **17** 056114
[11] Perkins R.J. *et al* 2012 *Phys. Rev. Lett.* **109** 045001
[12] Ono M. 1995 *Phys. Plasmas* **2** 4075
[13] Ryan P.M. *et al* 2001 *Fusion Eng. Des.* **56–57** 569
[14] Ryan P.M. *et al* 2011 *AIP Conf. Proc.* **1406** 101
[15] Raman R. *et al* 2001 *Nucl. Fusion* **41** 1081
[16] Kramer G. J. *et al* 2013 *Plasma Phys. Control. Fusion* **55** 025013
[17] Green D.L. *et al* 2011 *Phys. Rev. Lett.* **107** 145001
[18] Sabbagh S. *et al* 2001 *Nucl. Fusion* **41** 1601
[19] Menard J. 2006 private communication
[20] Watkins J.G. *et al* 1997 *J. Nucl. Mater.* **241–243** 645
[21] Perkins R.J. *et al* 2012 *39th EPS Conf. on Plasma Physics (Stockholm, Sweden, 2–6 July 2012)* vol 36F P-1.011 http://ocs.ciemat.es/epsicpp2012pap/pdf/P1.011.pdf
[22] Scotti F. *et al* 2012 *Rev. Sci. Instrum.* **83** 10E532
[23] Mastrovito D. *et al* 2003 *Rev. Sci. Instrum.* **74** 5090
[24] Herrmann A. *et al* 1995 *Plasma Phys. Control. Fusion* **37** 17
[25] Herrmann A. *et al* 2001 *28th EPS Conf. on Plasma Physics (Madeira, Portugal, 18–22 June 2001)* vol 25 p 2109 http://epsppd.epfl.ch/Madeira/html/pdf/P5.104.pdf
[26] Colas L. *et al* 2007 *J. Nucl. Mater.* **363–365** 555
[27] Bobkov Vl.V. *et al* 2010 *Nucl. Fusion* **50** 035004
[28] Noterdaeme J.-M. *et al* 1990 *Fusion Eng. Des.* **12** 127
[29] Wukitch S. *et al* 2007 *AIP Conf. Proc.* **933** 75
[30] Wukitch S. *et al* 2007 *J. Nucl. Mater.* **363–365** 491